MODAL ANALYSIS OF ROUGHNESS-INDUCED CROSSFLOW VORTICES IN A FALKNER–SKAN–COOKE BOUNDARY LAYER

Mattias Brynjell-Rahkola
Linné FLOW Centre and
Swedish e-Science Research Centre (SeRC)
KTH Mechanics, Royal Institute of Technology
SE-100 44 Stockholm, Sweden
mattiasbr@mech.kth.se

Philipp Schlatter
Linné FLOW Centre and
Swedish e-Science Research Centre (SeRC)
KTH Mechanics, Royal Institute of Technology
SE-100 44 Stockholm, Sweden
pschlatt@mech.kth.se

Ardeshir Hanifi
Linné FLOW Centre and
Swedish e-Science Research Centre (SeRC)
KTH Mechanics, Royal Institute of Technology
SE-100 44 Stockholm, Sweden
Swedish Defense Research Agency, FOI
SE-164 90 Stockholm, Sweden
ardeshir.hanifi@foi.se

Dan S. Henningson
Linné FLOW Centre and
Swedish e-Science Research Centre (SeRC)
KTH Mechanics, Royal Institute of Technology
SE-100 44 Stockholm, Sweden
henning@mech.kth.se

ABSTRACT

A three-dimensional global stability analysis using high-order direct numerical simulations is performed to investigate the effect of surface roughness with Reynolds number (based on roughness height) Re_k above and below the critical value for transition, on the eigenmodes of a Falkner–Skan–Cooke boundary layer. The surface roughness is introduced with the immersed boundary method and the eigenvalues and eigenfunctions are solved using an iterative time-stepper method. The study reveals a global instability for the case with higher Reynolds number that causes the flow in the non-linear simulations to break down to turbulence shortly downstream of the roughness. Examination of the unstable linear global modes show that these are the same modes that are observed in experiments immediately before breakdown due to secondary instability, which emphasizes the importance of these modes in transition.

INTRODUCTION

During the last decades, laminar-turbulent transition on swept airplane wings has received considerable attention. These flows, commonly known as the Falkner–Skan–Cooke (FSC) boundary layers, have a constant free-stream velocity in spanwise direction and an accelerating/decelerating velocity in streamwise direction, which causes the inviscid streamlines to be curved. In the inviscid region a balance between centrifugal and pressure forces exists, but inside the boundary layer, where the streamwise velocity decreases considerably, a force imbalance arises that generates a secondary flow called crossflow (Saric *et al.*, 2003). The crossflow component is perpendicular to the inviscid streamline and found to be inflectionally unstable (Gregory *et al.*, 1955). The commonly observed transition route for FSC boundary layers, at low free-stream turbulence, thus involves triggering of this primary instability by sufficiently large surface roughness that causes steady crossflow vortices to develop. These are in turn sensitive to secondary instabilities, that if triggered will lead to a very rapid breakdown to turbulence (White & Saric, 2005).

The specific transition scenario is ultimately determined by the disturbance environment and the boundary layer receptivity, *i.e.* the mechanisms by which disturbances enter into the boundary layer (see *e.g.* Tempelmann *et al.*, 2012 for boundary layer receptivity to surface roughness). Regarding excitation of crossflow vortices, surface roughness has been shown to be very efficient although several parameters such as location, height and diameter of the roughness impacts the final transition location (Radeztsky Jr. *et al.*, 1999). For roughness deeply submerged in the boundary layer, a roughness Reynolds number Re_k based on the height and undisturbed local velocity at the height of the roughness may be used to characterize the local flow conditions. While crossflow vortices have been found to be convectively unstable (Wassermann & Kloker, 2002), results for two-dimensional boundary layers (von Doenhoff & Braslow, 1961) suggest that there should exist a critical Re_k for which the disturbances introduced and eddies shed from the roughness would be strong enough to bypass the natural transition route (described above for three-dimensional boundary layers) and hence lead to an immediate breakdown to turbulence. Such phenomena could possibly arise in the presence of a wake instability that would cause the flow to be globally unstable.

Due to an intense research within the area, several studies have considered the susceptibility of crossflow vortices to secondary instabilities (see the review by Saric *et al.*, 2003) as well as the global instability of leading-edge flows and separation bubbles developing on airfoils (see the review by Theofilis, 2011). However, there is to our knowl-

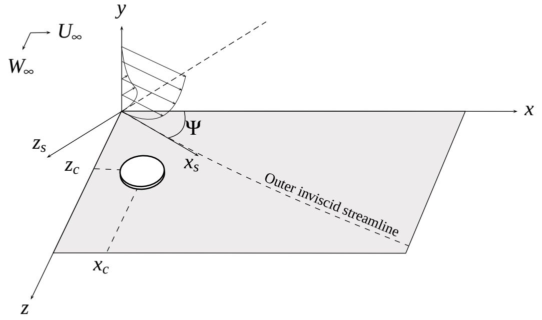

Figure 1: Sketch showing the setup of the simulations.

edge no printed work considering the impact of different roughness heights on the eigenmodes and eigenvalues of the flow, as well as the possibility of a global instability for a certain surface roughness. Recent advances in capabilities of numerical simulations allow us to study this problem using a three-dimensional global stability analysis, by which the flow is allowed to have three inhomogeneous spatial directions. Specifically, we investigate the global modes of a flow developing behind a three-dimensional roughness element as the roughness height and thus Re_k is increased from a sub-critical state characterized by laminar crossflow vortices into a super-critical state with a developing turbulent flow. The roughness Reynolds number is here defined as $Re_k = (u_k^{*2} + w_k^{*2})^{1/2} k^*/\nu$ with u_k^* and w_k^* being local velocities[1] at the roughness height, k. Also, the local Reynolds number is defined to be $Re_{\delta^*} = U_\infty^* \delta^*/\nu$, with δ^* being the local displacement thickness and U_∞^* the streamwise free-stream component. All the quantities are non-dimensionalized using the displacement thickness (δ_0^*) and the free-stream velocity (U_0^*) in the beginning of the box (subscript zero). A schematic picture illustrating the setup is shown in figure 1.

NUMERICAL METHOD

The study considers the time-dependent incompressible Navier–Stokes equations subject to constant fluid properties,

$$\frac{\partial \mathbf{u}}{\partial t} + \mathbf{u} \cdot \nabla \mathbf{u} = -\nabla p + \frac{1}{Re_{\delta_0^*}} \nabla^2 \mathbf{u} + \mathbf{f} \qquad (1)$$

$$\nabla \cdot \mathbf{u} = 0, \qquad (2)$$

where $Re_{\delta_0^*}$ denotes the Reynolds number in the beginning of the box. These equations are solved using the DNS code `nek5000` (Fischer *et al.*, 2008) based upon the spectral-element method (SEM) (Patera, 1984) which provides efficient parallelization and high-order accuracy. Within `nek5000` the equations are solved using a Galerkin method, where the domain is discretized by Legendre spectral-elements employing $N+1$ Gauss-Lobatto-Legendre (GLL) internal quadrature points and N^{th}-order Lagrange interpolation polynomials as base functions. Following the SEM $\mathbb{P}_N - \mathbb{P}_{N-2}$ discretization (Maday & Patera, 1989), the pressure field is solved using Lagrange interpolation polynomials of two orders less than the velocity field, which is $N = 7$. The equations are advanced in time using a conditionally stable backward differentiation and extrapolation scheme (BDFk/EXTk), employing an implicit treatment of the diffusion term and an explicit treatment of the convection term (Karniadakis *et al.*, 1991). The order of the time-stepping scheme is third order for the non-linear DNS and second order for the linear Arnoldi runs.

The computational domain for the simulations consists of a rectangular box with dimensions $420 \times 20 \times 25.14$ (expressed in terms of δ_0^*). As initial condition and boundary condition at the inflow, the FSC boundary layer solution is used. The FSC solution is also used at the upper free-stream boundary together with the additional feature that fluid can exit across it. In the spanwise direction periodic conditions are assigned and at the wall an ordinary no-slip condition is used. At the outflow boundary, a stress-free condition is employed. However, in order to damp out spurious waves generated at the outflow, a *sponge region* is added at the downstream end of the box (last 70 units), where the flow is forced towards FSC. The spanwise and streamwise extent of the *physical box* thus becomes similar to those used by Högberg & Henningson (1998). Inside the region where the surface roughness is applied, a unit element length is employed in wall-parallel directions and in the wall-normal direction, an element length of 0.2 is used. Outside the roughness-region the elements are stretched smoothly towards the edges of the physical box according to hyperbolic cosine, yielding a total number of 174174 spectral elements and about 90 million GLL points.

Roughness implementation

The surface roughness is simulated through application of an immersed boundary method (Peskin, 2002) abbreviated IBM. In IBM a volume force is applied inside the region occupied by the obstacle to oppose the pressure and shear forces generated by the fluid impinging upon the surface, thus providing damping of the velocity and approximating the zero slip condition. The IBM exists in a wide variety of forms and has been extensively employed within simulations involving fluid-structure interaction (see Peskin, 2002 for a list of references). Although the method allows obstacles to be introduced in a fluid domain with relative ease, it will only satisfy the no-slip condition approximately, and depending on the implementation respond slowly to large velocity fluctuations thus making it unsuitable for highly unsteady flows.

The implementation chosen in this work involves a cylindrical roughness and is similar to that used by Goldstein *et al.* (1993) in the sense that the coordinates of the roughness coincide with the coordinates of the fluid and the forcing function is proportional to the fluid velocity. The force term is added to the right hand side of equation (1) and is given by

$$\mathbf{f}(\mathbf{x},t) = -A\chi(r,y)\mathbf{u}(\mathbf{x},t)f(t), \qquad (3)$$

where A is a scalar specifying the amplitude of the force, χ is a mask function describing the region where the force acts, and f is a function used to generate a smooth turn-on in time (see Appendix for a detailed description). The roughness element is placed in the beginning of the box, centered at $x_c = 20.59$, $z_c = 0$ (see figure 1). The radius of the roughness is held constant at $r = 3$ with a variable height k.

[1] An asterisk (*) is used to denote dimensional quantities.

STABILITY ANALYSIS

The stability analysis consists of two steps. Following the common perturbation decomposition ($\mathbf{u} = \mathbf{U} + \mathbf{u}'$) a steady state base flow is first solved for, about which the equations are linearized and the global eigenfunctions and eigenvalues of a linear perturbation are computed.

Base flow

As a base flow for the stability analysis an FSC boundary layer with saturated crossflow vortices is used (see Appendix for governing equations). As mentioned earlier, this boundary layer is characterized by a constant free-stream velocity in spanwise direction and favorable pressure gradient in streamwise direction that causes the free-stream to accelerate with downstream distance,

$$U_\infty^* = U_0^* \left(\frac{x^*}{x_0^*}\right)^m \tag{4}$$

$$W_\infty^* = W_0^*. \tag{5}$$

The parameter m describes the acceleration of the flow and is related to the Hartree-parameter $\beta_H = 2m/(1+m)$, which can be thought of as a dimensionless pressure gradient. The numerical parameter values used in this work are similar to those used by Högberg & Henningson (1998), *i.e.* inflow Reynolds number $Re_{\delta_0^*} = 337.9$, distance from the leading edge to the beginning of the box $x_0 = 354.0$, spanwise free-stream velocity $W_0 = 1.442$ and acceleration parameter $m = 0.34207$.

To obtain a time-invariant solution of the base flow in the presence of the roughness element, the method of selective frequency damping (SFD) is used. This method was introduced by Åkervik *et al.* (2006) and forces the flow towards a temporally low-pass filtered solution, by adding a proportional forcing term to the right-hand side of equation (1), $-\chi_{SFD}(\mathbf{u} - \bar{\mathbf{u}})$. As a measure of convergence the ℓ^2-norm of the force amplitude inside the domain is used, with the convergence criterion $\mathscr{O}(10^{-12})$.

Global modes and time-stepper method

By assuming a time independent base flow $\bar{\mathbf{q}}$, the general initial-value problem reads

$$\mathscr{B}\frac{\partial \mathbf{q}'}{\partial t} = \mathscr{A}(\bar{\mathbf{q}}, Re)\mathbf{q}', \tag{6}$$

where the perturbation vector is $\mathbf{q}'(x,y,z,t) = (u',v',w',p')^T$. By retaining only the velocity components of the perturbation, the global modes become $\tilde{\mathbf{q}}' = \hat{\mathbf{q}}(x,y,z)e^{-i\omega t}$, with the eigenfunctions $\hat{\mathbf{q}} = (\hat{u},\hat{v},\hat{w})^T$. Upon applying a numerical discretization of the operators $\mathscr{B}$ and $\mathscr{A}$, equation (6) together with the global mode assumption can be expressed as the generalized eigenvalue problem

$$\mathbf{A}\hat{\mathbf{q}} = -i\omega\mathbf{B}\hat{\mathbf{q}}, \tag{7}$$

in which $\omega \in \mathbb{C}$ so that $\Re(\omega)$ gives the frequency of a given mode and $\Im(\omega)$ the growth rate ($\Im(\omega) < 0$ damped mode, $\Im(\omega) > 0$ amplified mode).

Due to the size of the computational mesh, solution of equation (7) using direct methods would render the problem extremely expensive and the requirements for storing the matrices tremendous. To overcome this, the eigenvalue problem (7) is solved using the implicitly restarted Arnoldi method (IRAM) from the ARPACK library (Lehoucq *et al.*, 1997). This method is based on an iterative time-stepping algorithm where the matrices of the full system are projected onto a Krylov subspace whose rank is orders of magnitude lower than that of the full system. This space is spanned by snapshots that are separated by equidistant time intervals and obtained by repeated application of an evolution operator. In order to avoid aliasing and for the eigenmodes of the Krylov space to also be the eigenmodes of the full system, temporal separation between the snapshots must be chosen such that the dynamics of the full system is captured. For a more complete discussion on the backgrounds of the method, the reader is referred to Bagheri *et al.* (2009), Theofilis (2011) and the references therein. In the present study the size of the Krylov space is $m = 250$, the snapshots are separated by 25 timesteps and the 50 most unstable eigenmodes are solved with an iteration tolerance of 10^{-6}. The boundary conditions of the perturbation at the inflow, outflow (sponge is retained) and free-stream boundary are set to homogeneous Dirichlet conditions.

RESULTS

Non-linear direct numerical simulations

By simulating non-linearly the flow in a smaller domain with various roughness heights, the critical point of transition is found to be located between $k = 0.9$ and $k = 1.1$. These heights correspond to Reynolds numbers $Re_k = 233.96$ and $Re_k = 338.86$ with shape parameters $d/k = 6.67$ and $d/k = 5.45$, which are in line with the transitional values reported by von Doenhoff & Braslow (1961) for two-dimensional flows. To get an overview of the frequencies present in the flow, a probe is positioned in the super-critical wake at a distance 20.42 from the roughness center. The frequency spectrum (figure 2) reveals the presence of a highly amplified fundamental frequency together with its higher harmonics. The energy level of the fundamental frequency ($\omega = 0.813$) is much higher than those of the harmonics, which suggests that this frequency is strongly amplified by the roughness and thus important in the onset of transition. The temporal evolution of the fundamental frequency and its first harmonic ($\omega = 1.622$) recorded by the probe in the super- and sub-critical cases are shown in figure 3. Clearly, the frequencies in the sub-critical case after an initial transient period experience an exponential decay with rate approximately 0.015 whereas the corresponding frequencies in the super-critical case after the transient phase grows and saturates at a constant amplitude. The critical Re_k at which transition due to roughness occurs must therefore be encircled by these two heights. The resulting three-dimensional flow fields are shown in figure 4.

Modal analysis

Given the frequency spectrum of figure 2, two simulations having different timesteps ($dt = 7.5 \cdot 10^{-3}$ and $dt = 3.75 \cdot 10^{-3}$) and thus different CFL-numbers (approximately 0.3 and 0.15) are performed. The temporal separation between the snapshots of the Krylov space is chosen to yield approximately 20 respectively 40 samples in the pe-

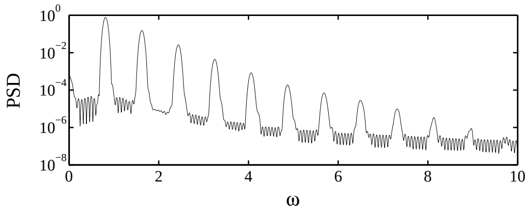

Figure 2: Frequency spectrum in the roughness wake, $k = 1.1$.

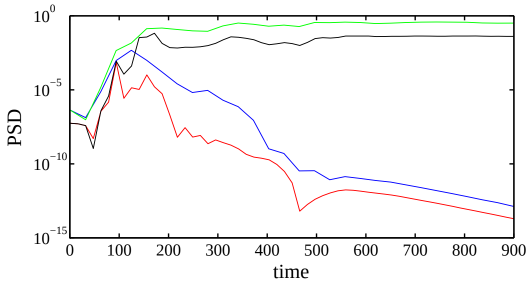

Figure 3: Temporal evolution of $\omega = 0.813$ for super-critical (–) and sub-critical (–) roughness, as well as $\omega = 1.622$ for super-critical (–) and sub-critical (–) roughness.

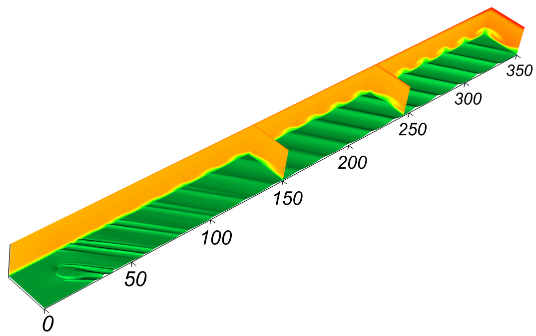

(a) Sub-critical roughness, $k = 0.9$.

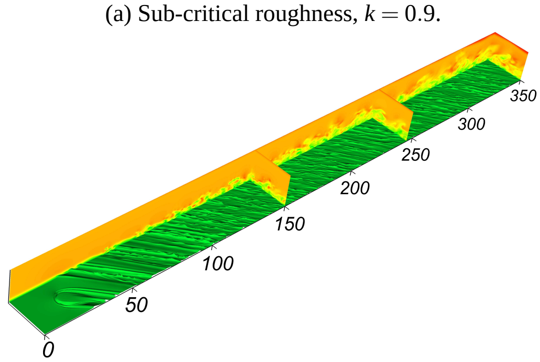

(b) Super-critical roughness, $k = 1.1$.

Figure 4: Streamwise component of flow developing behind the roughness. Velocity contour corresponds to $u = 0.3$ and cross-sectional planes are positioned at $x = 150, 245, 350$.

riod of $\omega = 1.622$, and the resulting eigenvalues are shown on the right and left half-planes of figure 5 (eigenvalues and eigenfunctions appear in complex conjugate pairs, requiring only half the spectrum to be plotted). Since the number of snapshots in both cases should be sufficient to resolve the dynamics of the system, no aliasing (Bagheri *et al.*, 2009) is expected in either of the runs. Comparison of the eigenvalue spectrum from the two simulations reveals a slight dependancy on the CFL-number which becomes more pronounced for higher frequencies. Although the main features remain unchanged between the two runs, the results corresponding to the lower CFL-number has more distinct eigenvalue branches which would indicate these to be more accurate than the spectrum corresponding to higher CFL-number. The remaining part of this section will hence consider the results corresponding to CFL≈ 0.15.

Depending on energy production mechanism, eigenmodes may be classified as either *y-modes* or *z-modes* (Malik *et al.*, 1999) with y-modes being spatially confined to the overturning top region of the crossflow vortex and the z-modes being located on the upwelling frontal region. To clarify which of the eigenvalues correspond to which family of modes, the eigenvalues appearing in figure 5 have been colored such that red marks indicate z-modes, blue marks y-modes, magenta marks low-frequency modes, green marks stationary modes and black marks modes that cannot be clearly classified into either category. As such, it is seen that the modes appearing in the super-critical case are z-modes (figure 6a) and y-modes (figure 6b), with the mode having the highest growth rate being a z-mode. The frequencies corresponding to the two most unstable modes are $\omega_r = 0.8251$ and $\omega_r = 0.8095$, which are in very close agreement with the frequency obtained from the DNS ($\omega = 0.813$). For the sub-critical case, the least stable mode is a stationary mode having zero frequency (figure 6c). In addition to these and the z-modes, a low-frequency mode having frequency $\omega_r = 0.0688$ (figure 6d) is observed.

The eigenvalues marked in black correspond to eigenfunctions containing structures of both z- and y-modes (see figure 6e) with those having lower frequency featuring a more pronounced location towards the upwelling region of the vortex and those having higher frequency being located towards the overturning region. This shows that the shape of the eigenfunctions changes rather continuously from z-modes to y-modes with increasing frequency.

DISCUSSION AND CONCLUSIONS

A fully three-dimensional global stability analysis has been carried out using direct numerical simulations and an iterative time-stepper method based on the Arnoldi algorithm. The study is likely to be the first of its kind for the flowcase, and reveals a global instability as the roughness height (and Re_k) is increased from a sub-critical to a super-critical state.

The results of the sub-critical case verify the convective instability of the crossflow vortices found by Wassermann & Kloker (2002) and the least stable mode turns out to be a stationary mode. The z- and y-modes that become unstable in the super-critical case are in line with what is observed in experiments studying the breakdown due to secondary instability (White & Saric, 2005), where high-frequency modes qualitatively resembling either figure 6a or 6b are always observed to precede breakdown to turbulence. Results from previous studies along with the present modal analysis emphasize the importance of these modes for transition on swept wings. Furthermore the present results indicate which modes are most important to damp in flow control. Interesting is also to note the continuous shift from z- to

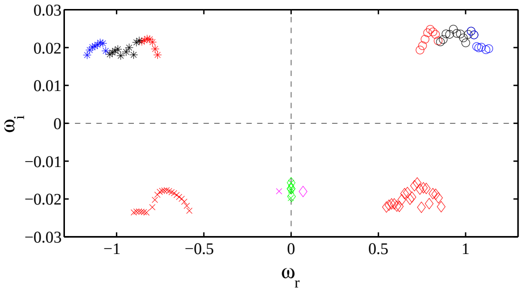

Figure 5: Eigenvalues. Right half (CFL≈ 0.3): Super-critical (○), sub-critical (◇); left half (CFL≈ 0.15): Super-critical (∗), sub-critical (×). Color-coding: z-modes – red, y-modes – blue, low-frequency modes – magenta, stationary modes – green, unclassified modes – black.

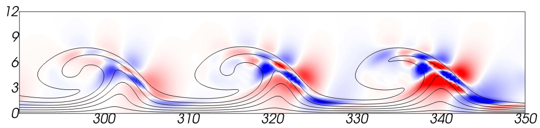

(a) Most unstable mode (z-mode), super-critical roughness.

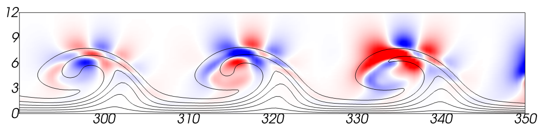

(b) Most unstable y-mode, super-critical roughness.

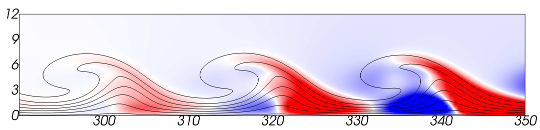

(c) Least stable mode (stationary), sub-critical roughness.

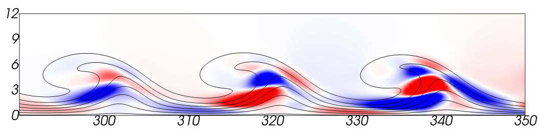

(d) Low-frequency mode, sub-critical roughness.

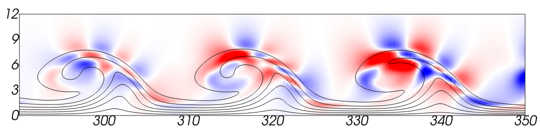

(e) Mode containing structures of both z- and y-modes, super-critical roughness.

Figure 6: Streamwise component ($\hat{u}$) of a selection of eigenmodes viewed in the xy-plane (CFL≈ 0.15). Negative values are colored in blue, positive in red, base flow contours are shown in black.

y-modes that takes place with increasing frequency.

Forcing of the roughness using IBM works well in the present case and provides damping of the velocity in the roughness center to $\mathscr{O}(10^{-4})$ for the streamwise and $\mathscr{O}(10^{-5})$ for the spanwise and wall-normal components. Although the geometrical flexibility of the SEM-code would allow the roughness to be meshed and the roughness representation hence to be more accurate, utilizing a direct forcing method can be a good way of decreasing the computational cost and is an important method to consider when performing expensive large-scale simulations.

This work furthermore highlights the sensitivity of this type of studies to both temporal and spatial resolution. Although the timestep in all performed simulations is far below the critical one for the time-stepping scheme, the details of the eigenvalue spectrum appears to be sensitive to this parameter (CFL-number). This could be an indication that the flow is marginally resolved in space (Peplinski *et al.*, 2012) and would therefore suggest an increase in polynomial order. However, such changes would drastically increase the cost of the simulations as the time per timestep is known to increase quadratically with polynomial order (N) and the stability analysis using $N = 7$ ($\sim$ 90 million grid points) lasted on average 5 days with 2048 cores.

ACKNOWLEDGMENTS

We would like to thank Adam Peplinski for providing the tools used in the stability analysis and sharing his experience in the area. All simulations has been performed at The National Supercomputer Centre in Sweden (NSC) with computer time granted by Swedish National Infrastructure for Computing (SNIC).

APPENDIX
FSC boundary layer equations

The similarity solutions of Falkner & Skan (1931) and Cooke (1950), subject to boundary conditions $f = f' = g = 0$ at $\eta = 0$ and $f' \to 1, g \to 1$ as $\eta \to \infty$, read

$$f''' + ff'' + \beta_H(1 - f'^2) = 0, \tag{8}$$
$$g'' + fg' = 0. \tag{9}$$

These equations are derived from Prandtl's boundary layer equation (see Schlichting, 1979) and are solved with shooting method using Newton–Raphson and fourth-order Runge–Kutta. By defining a stream function ψ^* and a dimensionless wall-normal coordinate η,

$$\psi^* = \sqrt{\frac{2}{m+1} x^* U^*_\infty \nu}\, f(\eta), \quad u^* = \frac{\partial \psi^*}{\partial y^*}, \quad v^* = -\frac{\partial \psi^*}{\partial x^*} \tag{10}$$

$$\eta = y^* \sqrt{\frac{m+1}{2} \frac{U^*_\infty}{\nu x^*}}, \tag{11}$$

the final base flow components can be written as

$$u = U_\infty f', \tag{12}$$
$$v = \frac{1}{2}\sqrt{\frac{2}{m+1} \frac{U_\infty}{x} \frac{1}{Re_{\delta^*_0}}} \left[(1-m) f'\eta - (1+m) f\right], \tag{13}$$
$$w = W_\infty g. \tag{14}$$

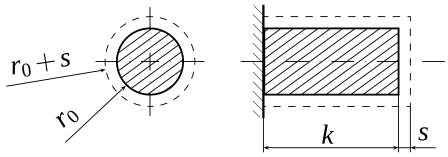

Figure 7: Sketch of the roughness with its defining parameters (rotated 90 degrees clockwise).

Roughness forcing functions

The mask function $\chi(r,y)$ varies continuously in the interval [0,1] and is unity inside the roughness with radius r_0 and height k, where $r = \left((x-x_c)^2+(z-z_c)^2\right)^{1/2}$. To diffuse the discontinuity introduced by the boundary, the value decreases smoothly to zero inside a smoothing region of width $s = 0.4$ right outside the roughness. Equation (15) and the accompanying figure 7 illustrate the shape of the roughness.

$$\chi(r,y) = \begin{cases} 0, & y \geq (k+s), \\ & r \geq (r_0+s) \\ 0.5\left[1+\cos\left(\frac{r-r_0}{s}\pi\right)\right]\cdot & k < y < (k+s), \\ 0.5\left[1+\cos\left(\frac{y-k}{s}\pi\right)\right] & r_0 < r < (r_0+s) \\ 0.5\left[1+\cos\left(\frac{r-r_0}{s}\pi\right)\right], & y \leq k, \\ & r_0 < r < (r_0+s) \\ 0.5\left[1+\cos\left(\frac{y-k}{s}\pi\right)\right], & k < y < (k+s), \\ & r \leq r_0 \\ 1, & y \leq k, \\ & r \leq r_0. \end{cases} \qquad (15)$$

The function $f(t)$ used to smooth the roughness in time is given by

$$f(t) = S(-t/t_{scale}) \qquad (16)$$

$$S(x) = \begin{cases} 0, & x \leq 0 \\ 1/\left[1+\exp\left(\frac{1}{x-1}+\frac{1}{x}\right)\right], & 0 < x < 1 \\ 1, & x \geq 1. \end{cases} \qquad (17)$$

REFERENCES

Åkervik, E., Brandt, L., Henningson, D. S., Hœpffner, J., Marxen, O. & Schlatter, P. 2006 Steady solutions of the Navier–Stokes equations by selective frequency damping. *Physics of Fluids* **18** (6).

Bagheri, S, Åkervik, E., Brandt, L. & Henningson, D. S. 2009 Matrix-Free Methods for the Stability and Control of Boundary Layers. *AIAA Journal* **47** (5), 1057–1068.

Cooke, J. C. 1950 The boundary layer of a class of infinite yawed cylinders. *Mathematical Proceedings of the Cambridge Philosophical Society* **46** (04), 645–648.

von Doenhoff, A. E. & Braslow, A. L. 1961 The effect of distributed surface roughness on laminar flow. In *Boundary layer and Flow Control: its Principles and Application* (ed. G.V. Lachmann), pp. 657–681. Pergamon Press.

Falkner, V. M. & Skan, S. W. 1931 Some approximate solutions of the boundary layer equations. *Philosophical Magazine and Journal of Science* **12** (80), 865–896.

Fischer, P. F., Lottes, J. W. & Kerkemeier, S. G. 2008 nek5000 Web page. http://nek5000.mcs.anl.gov.

Goldstein, D., Handler, R. & Sirovich, L. 1993 Modeling a no-slip flow boundary with an external force field. *Journal of Computational Physics* **105** (2), 354–366.

Gregory, N., Stuart, J. T. & Walker, W. S. 1955 On the stability of three-dimensional boundary layers with application to the flow due to a rotating disk. *Philosophical Transactions of the Royal Society of London. Series A, Mathematical and Physical Sciences* **248** (943), 155–199.

Högberg, M. & Henningson, D. 1998 Secondary instability of cross-flow vortices in Falkner-Skan-Cooke boundary layers. *Journal of Fluid Mechanics* **368**, 339–357.

Karniadakis, G. E., Israeli, M. & Orszag, S. A. 1991 High-order splitting methods for the incompressible Navier–Stokes equations. *Journal of Computational Physics* **97** (2), 414–443.

Lehoucq, R. B., Sorensen, D. C. & Yang, C. 1997 ARPACK User's Guide: Solution of Large Scale Eigenvalue Problems by Implicitly Restarted Arnoldi Methods.

Maday, Y. & Patera, A. T. 1989 Spectral element methods for the Navier–Stokes equations. In *State of the Art Surveys in Computational Mechanics* (ed. A. K. Noor), pp. 71–143. New York: ASME.

Malik, M. R., Li, F., Choudhari, M. M. & Chang, C.-L. 1999 Secondary instability of crossflow vortices and swept-wing boundary-layer transition. *Journal of Fluid Mechanics* **399**, 85–115.

Patera, A. T. 1984 A spectral element method for fluid dynamics: Laminar flow in a channel expansion. *Journal of Computational Physics* **54** (3), 468 – 488.

Peplinski, A., Schlatter, P., Fischer, P.F. & Henningson, D. S. 2012 Stability Tools for the Spectral-Element Code Nek5000; Application to Jet-in-Crossflow. In *ICOSAHOM'12, International Conference on Spectral and High Order Methods*.

Peskin, C. S. 2002 The immersed boundary method. *Acta Numerica* **11**, 479–517.

Radeztsky Jr. R. H., Reibert, M. S. & Saric, W. S. 1999 Effect of isolated micron-sized roughness on transition in swept-wing flows. *AIAA Journal* **37** (11), 1370–1377.

Saric, W. S., Reed, H. L. & White, E. B. 2003 Stability and transition of three-dimensional boundary layers. *Annual Review of Fluid Mechanics* **35**, 413–440.

Schlichting, H. 1979 *Boundary-Layer Theory*, 7th edn. McGraw-Hill, Inc.

Tempelmann, D., Schrader, L.-U., Hanifi, A., Brandt, L. & Henningson, D. S. 2012 Swept wing boundary-layer receptivity to localized surface roughness. *Journal of Fluid Mechanics* **711**, 516–544.

Theofilis, V. 2011 Global linear instability. *Annual Review of Fluid Mechanics* **43** (1), 319–352.

Wassermann, P. & Kloker, M. 2002 Mechanisms and passive control of crossflow-vortex-induced transition in a three-dimensional boundary layer. *Journal of Fluid Mechanics* **456**, 49–84.

White, E. B. & Saric, W. S. 2005 Secondary instability of crossflow vortices. *Journal of Fluid Mechanics* **525**, 275–308.